

---

This is an electronic reprint of the original article.  
This reprint may differ from the original in pagination and typographic detail.

Hällström, L.; Koskinen, T.; Tossi, C.; Juntunen, T.; Tittonen, I.

## Multiphysics simulation explaining the behaviour of evaporation-driven nanoporous generators

*Published in:*  
Energy Conversion and Management

*DOI:*  
[10.1016/j.enconman.2022.115382](https://doi.org/10.1016/j.enconman.2022.115382)

Published: 15/03/2022

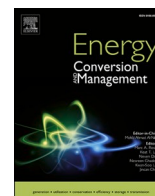
*Document Version*  
Publisher's PDF, also known as Version of record

*Published under the following license:*  
CC BY

*Please cite the original version:*  
Hällström, L., Koskinen, T., Tossi, C., Juntunen, T., & Tittonen, I. (2022). Multiphysics simulation explaining the behaviour of evaporation-driven nanoporous generators. *Energy Conversion and Management*, 256, Article 115382. <https://doi.org/10.1016/j.enconman.2022.115382>

---

This material is protected by copyright and other intellectual property rights, and duplication or sale of all or part of any of the repository collections is not permitted, except that material may be duplicated by you for your research use or educational purposes in electronic or print form. You must obtain permission for any other use. Electronic or print copies may not be offered, whether for sale or otherwise to anyone who is not an authorised user.



# Multiphysics simulation explaining the behaviour of evaporation-driven nanoporous generators

L. Hällström<sup>\*</sup>, T. Koskinen, C. Tossi, T. Juntunen, I. Tittonen

Department of Electronics and Nanoengineering, Aalto University, Espoo, PL 13500, Finland

## ARTICLE INFO

### Keywords:

Nanoporous carbon  
Streaming current  
Generator  
Finite-element method  
Simulation

## ABSTRACT

Evaporation-induced electricity generation in porous nanomaterials has recently attracted considerable attention due to relatively high produced voltages and wide operating conditions. Here, we present a combined study of computational and experimental work exploiting finite-element method simulations to find the critical parameters influencing the performance of such generators. The simulated behaviour is found to agree with the experimental data within typical variation of the measurements. We find that the electrical power produced by the generator depends not only on the properties of the porous material, but also on the surrounding environment of the generator. Particularly, the pore size and geometry are found to have a significant influence on the output power, highlighting the importance of accurate characterization of the samples and careful control of the laboratory conditions when performing experimental work. Increasing the pore size from 5 to 20 nm improves the simulated output voltage from 0.12 to 0.47 V, while increasing the ambient humidity to 100% will prevent voltage generation completely. The obtained results can guide the future design of generators based on water evaporation induced capillary flow in a nanoporous carbon black film, leading to more efficient power production.

## 1. Introduction

In recent years, increasing interest has emerged in generating electric power from the interaction between water and functionalized nanomaterials [1–3]. An extensively studied class of these generators produces electricity from the streaming current created by evaporation-driven capillary water flow in a porous material: the continuous water flow through the device generates an electrical current, which can be harvested and used to power external devices [4–6]. While the concept of streaming current has been known since 1861 [7], the application of using porous carbon materials for power generation was first demonstrated in 2017 by Xue et al. [6]. Since then, different materials have been tested with varying efficiencies, with current state-of-the-art approaches producing voltages of up to 5 V [8]. In addition to porous carbon, other viable materials have been demonstrated, such as biological nanofibrils [9], nanostructured silicon [10] and natural wood [11,12]. These materials have been used with various device geometries, including floating and three-dimensional large-volume structures [13,14]. Porous carbon materials present the advantages of being abundant, economically competitive, non-toxic, and scalable [15]. The use of water evaporation as a driving force for a hydrovoltaic generator

can exploit the latent heat from present instrumentation or from factory elements, offering an efficient way to recycle waste heat in industrial infrastructure. Alongside the efforts in material development [10], proposed applications span from wearable electronics [16–19] to low-power IoT devices [18], exploiting different methods such as plasmonic heating or composite polymers to improve the evaporation rate and power generation in the device [20,21].

Water transport and evaporation in porous materials has been extensively studied [22–27] and applied for example in food and earth sciences [28–30], and the theory has since been applied to solar steam generation with porous materials [31]. However, the connection between the water evaporation and electricity generation in a porous film remains poorly understood. Although the microscopic mechanism of the water flow and subsequent generation of streaming current inside the capillary channels of porous materials has been studied both via first-principles and in experimental settings [32,33,6], little work has been conducted to understand the underlying physics of the porous material on the scale of complete devices, even if such information is crucial for the design and optimization of large-scale implementations of evaporation-powered nanogenerators.

Here, we present a combined study of computational and experimental results explaining the influence of the key physical phenomena

<sup>\*</sup> Corresponding author.

<https://doi.org/10.1016/j.enconman.2022.115382>

Received 15 November 2021; Received in revised form 20 January 2022; Accepted 11 February 2022

Available online 25 February 2022

0196-8904/© 2022 The Author(s). Published by Elsevier Ltd. This is an open access article under the CC BY license (<http://creativecommons.org/licenses/by/4.0/>).

**Nomenclature***Latin Letters*

$g$	gravitational acceleration ( $\text{m s}^{-2}$ )
$A$	cross section area ( $\text{m}^2$ )
$a_w$	water activity
$C_j$	streaming current coefficient ( $\text{A s m}^{-3}$ )
$c_{sat_0}$	vapor saturation concentration in air ( $\text{mol m}^{-3}$ )
$c_{sat}$	vapor saturation concentration ( $\text{mol m}^{-3}$ )
$c_{va}$	vapor concentration ( $\text{mol m}^{-3}$ )
$D_{eff}$	effective vapor diffusion coefficient ( $\text{m}^2 \text{s}^{-1}$ )
$D_{va}$	vapor diffusion coefficient ( $\text{m}^2 \text{s}^{-1}$ )
$G$	conductance (S)
$I_s$	streaming current (A)
$j_i$	current source (A)
$K$	evaporation rate constant ( $\text{s}^{-1}$ )
$k$	thermal conductivity ( $\text{W m}^{-1} \text{K}^{-1}$ )
$P$	pressure (Pa)
$Q$	volumetric flux ( $\text{m s}^{-1}$ )
$r_c$	critical pore radius (m)
$S_g$	gas phase saturation
$S_l$	liquid phase saturation
$T$	temperature (K)

$t$	time (s)
$T_0$	ambient temperature (K)
$u_0$	mean airflow velocity ( $\text{m s}^{-1}$ )
$u_y$	liquid velocity y-component ( $\text{m s}^{-1}$ )
$V$	electric potential (V)
$\mathbf{u}_l$	liquid phase flow velocity ( $\text{m s}^{-1}$ )
$\mathbf{u}_g$	gas phase flow velocity ( $\text{m s}^{-1}$ )

*Greek Letters*

$\bar{\mu}$	effective viscosity (Pa s)
$\bar{\rho}$	effective density ( $\text{kg m}^{-3}$ )
$\kappa$	permeability ( $\text{m}^2$ )
$\kappa_{rg}$	gas phase relative permeability
$\kappa_{rl}$	liquid phase relative permeability
$\lambda$	pore size distribution index
$\mu_g$	gas phase viscosity (Pa s)
$\mu_l$	liquid phase viscosity (Pa s)
$\phi$	relative humidity
$\rho_g$	gas phase density ( $\text{kg m}^{-3}$ )
$\rho_l$	liquid phase density ( $\text{kg m}^{-3}$ )
$\sigma_{va}$	vapor mass source ( $\text{kg m}^{-3} \text{s}^{-1}$ )
$\sigma_l$	liquid mass source ( $\text{kg m}^{-3} \text{s}^{-1}$ )
$\varphi$	porosity

in thin-film capillary hydrovoltaic devices. We utilize a finite-element method simulation to reproduce the results from experimental devices and to further study the effects of the key parameters on the produced voltage. The simulation reveals in detail the dynamics of the multiphase water flow, and the results are used to identify the most critical parameters for maximizing the power output. In particular, the porosity and pore structure of the carbon film are found to have a significant effect on the power output.

**2. Methods****2.1. Experimental**

The porous carbon material was fabricated using ink prepared from toluene soot: the toluene was burned in an alcohol burner, and the produced soot was collected onto a metal plate. From the plate, 800 mg of toluene soot were removed and mixed in a beaker with 400 mg of ethyl cellulose (48% ethoxyl), 8 ml of terpineol (mixture of isomers) and 40 ml of methanol (Sigma–Aldrich). The beaker was then placed on a magnetic stirring plate while kept at a temperature of 75 °C for three

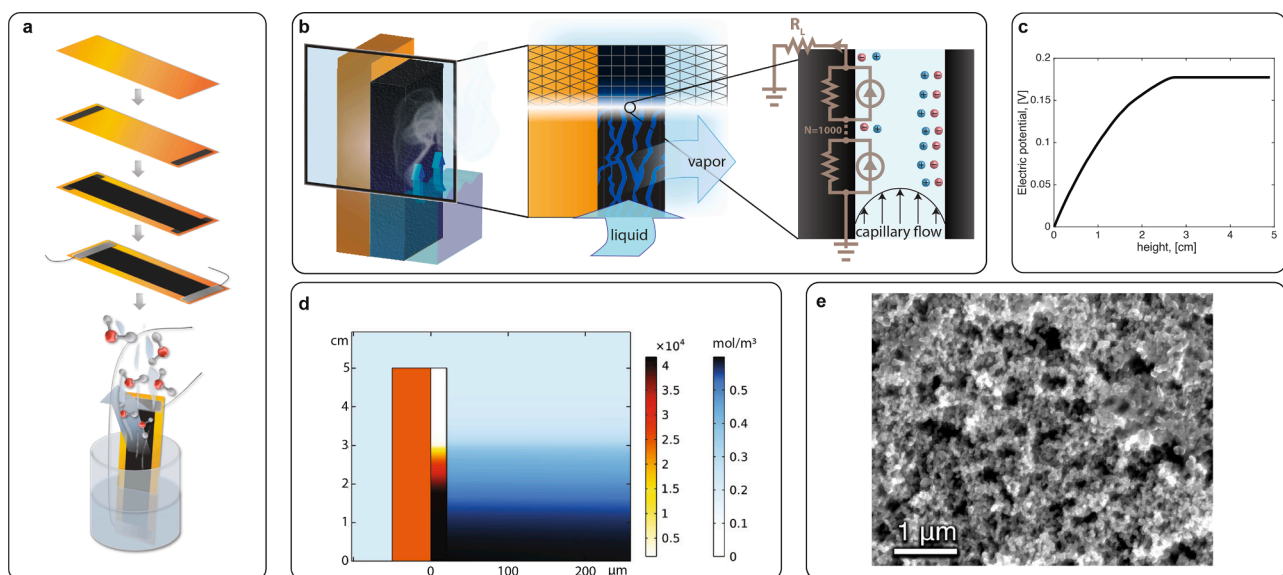


**Fig. 1.** a) Fabrication process of the device. The electrodes are painted first, followed by the porous layer. b) Illustration of the simulation process: A 2D cross section of the device is modelled using FEM, solving the liquid water and vapor fluxes in the porous material. The liquid flowrate is further applied to an equivalent electrical circuit to compute the electrical power output. c) The simulated steady state electrical potential vs. the distance from the water surface in the device. d) Steady state of the FEM simulation of the water dynamics. Liquid water is represented by the red gradient, and water vapor by the blue gradient. The uniform orange area represents the Kapton substrate. e) SEM image of the sample surface.

hours in order to create a homogenous slurry.

Fig. 1 (a) illustrates the device fabrication process: First, PELCO® colloidal graphite was used to paint electrodes on flexible Kapton® polyimide substrates. After the electrodes were dry, the slurry was deposited on the substrates with a 3D-printed coater: the deposition resulted in 15 mm wide and 50 mm long films, which were subsequently placed in a 120 °C oven for 1 h to evaporate the solvent. After the treatment, the films were annealed on a hot plate at 375 °C for 1 h to remove the ethyl cellulose binder. Electrical wiring was then attached using colloidal graphite. After the wiring had adhered and the colloidal graphite had dried, the electrodes were sealed with a transparent two-component epoxy. The recipe is based on the original recipe used by Xue et al. [6].

The device was then attached into a supportive piece of plastic, which was placed in a beaker partially filled with water. The electrical wiring was connected to a source-meter (Keithley 2602B) and current-voltage characteristics were recorded to determine the open-circuit voltage and device resistance at different times under operation.

The thickness of the carbon layer was measured from crosscut SEM images, with a range of 5-20 μm; an example image is shown in Supplementary Fig. S1. Density and true volume of the samples were measured using a helium pycnometer (Quantachrome Ultrapyc 1200e). The measured density of 2276 kg/m<sup>3</sup> is comparable to reported values for similar materials [35].

## 2.2. Water dynamics model

The simulation implemented in this work is a 2D cross-sectional model of the device with the geometry as shown in Fig. 1 (b and d): the device stands vertically in air with the water entering from the bottom and evaporating towards the right. On the left side of the porous material is the Kapton substrate, which acts as an impermeable barrier for both liquid and vapor flow. Inside the porous material the model solves the two-phase fluid flow, where liquid water rises driven by capillary force, and the rest of the space is occupied by a gas phase. The gas phase consists of air and water vapor, which can freely flow out of the porous material. Capillary action draws water from the reservoir into the porous material, while the water simultaneously evaporates and the vapor is removed by diffusion and convection. The input parameters of the simulation are presented in Table 1. The liquid and gas phases are connected by a saturation constraint

$$S_g + S_l = 1 \quad (1)$$

where  $S_g$  is the saturation of the gas phase and  $S_l$  the saturation of the liquid phase. The liquid phase is always entirely liquid water, while the gas phase represents moist air that can have varying amounts of water vapor in it. Therefore, in addition to solving the liquid and gas phase saturations, the water vapour concentration in the gas phase must be

**Table 1**  
Simulation parameters

Symbol	Value	Description
$C_j$	$4.5 \times 10^4$ A s/m <sup>3</sup>	Streaming current coefficient
$D_{va}$	$2.6 \times 10^{-5}$ m <sup>2</sup> /s	Water vapor diffusion coefficient
$k$	0.3 W/m K [34]	Thermal conductivity
$K$	10000 s <sup>-1</sup>	Evaporation rate constant
$r_c$	7 nm	Critical pore radius
$R_{s,dry}$	1.7 M Ω/ □	Sry sheet resistance
$R_{s,humid}$	2.7 M Ω/ □	Humid sheet resistance
$R_{s,wet}$	0.85 M Ω/ □	Wet sheet resistance
$T_0$	22 °C	Ambient temperature
$u_0$	0.05 m/s	Airflow velocity
$\lambda$	1	Pore size distribution index
$\varphi$	0.75	Porosity
$\phi$	0.2	Ambient relative humidity
$\rho$	2276 kg/m <sup>3</sup>	Material density

tracked separately. The operation of the device is tied to the flow of water through the porous material, so the key variables to be solved are the liquid water and water vapor concentrations and the respective volumetric fluxes. These are solved as functions of the position in the device and of time with an FEM simulation implemented in COMSOL Multiphysics®. The transport of water inside the porous material is described by a two-phase transport model, and the water vapor in the air by a diluted species transport model. Additionally, these models are self-consistently coupled to a temperature simulation that includes the effects of convection, thermal conduction and evaporative cooling. The material parameters used for the porous carbon layer are listed in Table 1. For water and air, built-in material models from COMSOL were used. The simulation uses Darcy's law to calculate the flow of the liquid phase in the porous media, where the flow is given by

$$\mathbf{u}_l = -\frac{\kappa}{\bar{\mu}}(\nabla P + \bar{\rho}\mathbf{g}), \quad (2)$$

where  $\mathbf{u}_l$  is the Darcy velocity for the liquid flow,  $\kappa$  the mechanical permeability of the porous material,  $P$  the pressure and  $\mathbf{g}$  the gravitational acceleration. Eq. 2 extends Darcy's law to multiphase flow by defining the effective density  $\bar{\rho}$  and the effective viscosity  $\bar{\mu}$  of the liquid-air mixture. The effective density is the mean of the densities of the liquid and gas phases, weighted by the saturations of the two phases

$$\bar{\rho} = S_l\rho_l + S_g\rho_g, \quad (3)$$

and the effective viscosity of the liquid-gas mixture is given by

$$\bar{\mu} = \frac{\bar{\rho}}{\frac{\kappa_l\rho_l}{\mu_l} + \frac{\kappa_g\rho_g}{\mu_g}}. \quad (4)$$

Here  $\kappa_l$  and  $\kappa_g$  are the relative permeabilities of the porous material for the liquid and gas phases respectively, and they are defined as functions of the liquid phase saturation:

$$\kappa_l = S_l^2, \quad (5)$$

$$\kappa_g = (1 - S_l)^2. \quad (6)$$

The viscosity of the liquid-gas mixture is high when the liquid saturation is close to 50%, resulting in high pressure gradient and therefore high Darcy velocity close to the wetting front, where the porous medium is only partially saturated by water.

The permeability in Eq. 2 describing the sensitivity of the liquid flowrate to the pressure gradient is defined by

$$\kappa = \varphi \frac{r_c^2}{4}, \quad (7)$$

where  $\varphi$  is the porosity of the porous material, with larger values signifying more empty space in the material, and the constant factor 1/4 accounts for pore geometry and tortuosity [36,37]. The symbol  $r_c$  refers to the critical pore radius, which is the smallest radius of the pore the water is flowing through.

The velocity field  $\mathbf{u}$  from Darcy's law given by Eq. 2 is then used in the transport equation for the liquid phase

$$\frac{\partial}{\partial t} \varphi \rho_l S_l + \nabla \cdot (\rho_l \mathbf{u}_l) = \sigma_l. \quad (8)$$

The right hand side term  $\sigma_l$  describes liquid water sources and sinks, which in this case include the evaporation of water from the device. The evaporation rate of water is a linear function of the vapor concentration

$$\sigma_l = -K(a_w c_{sat} - c_{va}), \quad (9)$$

where  $K$  is the reaction rate constant,  $a_w$  the water activity and  $c_{va}$  the water vapor concentration in the gas phase. In this work, we assume that the reaction rate is fast compared to the water vapor flow, so that the

evaporation rate is mass transport limited. The activity of water  $a_w$  is defined as a function of the moisture content, interpolating from the data by Brennan et al. [38]. The activity curve is shown in Supplementary Fig. S3. The saturation concentration in the open air domain,  $c_{sat_0}$ , is given by an analytic approximation based on the Tetens equation and the ideal gas law [39]

$$c_{sat_0} = 610.7 [Pa] 10^{7.5 \frac{T - 273.15 [K]}{T - 35.85 [K]}} \frac{1}{RT}. \quad (10)$$

Warmer air is able to hold more moisture, and higher saturation concentrations in Eq. 9 lead to higher evaporation rates. As the evaporation of water directly affects the surrounding temperature via evaporative cooling, the temperature has to be solved self-consistently with the rest of the simulation. Inside the porous medium the saturated vapor concentration additionally depends on the effective volume available for the water vapor, defined by the porosity and the gas phase saturation

$$c_{sat} = c_{sat_0} \varphi S_{ma}. \quad (11)$$

The vapor phase flow follows the convection–diffusion equation for mass conservation both inside the porous medium and in the outside air

$$\frac{\partial c_{va}}{\partial t} + \mathbf{u}_g \nabla c_{va} + \nabla \cdot (-D_{va} \nabla c_{va}) = \sigma_v a. \quad (12)$$

The velocity field  $\mathbf{u}_g$  is given by the ambient air flow, which is solved separately before the fluid dynamic simulation as a stationary solution assuming laminar air flow. The air flow profile is shown in Fig. 2. Inside the porous medium the vapor diffusion coefficient  $D_{va}$  is replaced by the effective diffusion coefficient  $D_{eff}$ , defined according to the Millington and Quirk equation [40–42]

$$D_{eff} = D_{va} S_g^{10/3} \varphi^{4/3}. \quad (13)$$

In practice, the convective flow velocity inside the porous material turns out to be negligible, and the vapor movement is due to diffusion only. The reaction term  $\sigma_{va}$  describes the vapor generated as the water evaporates, and is related to the liquid reaction rate by  $\sigma_g = -\sigma_l$  so that the total water mass is conserved. The boundary conditions used for all of the interfaces in the simulation are described in detail in Supplementary material Section 2.

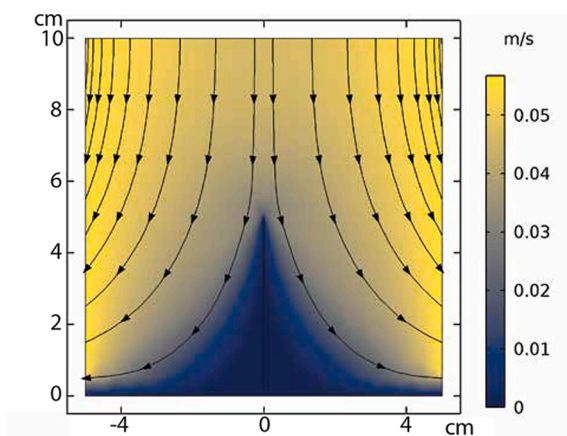


Fig. 2. The stationary solution for the ambient air flow used during the time evolution simulation. The sample is in the middle, viewed from the same orientation as in Fig. 1 (d), but scaled to show the full simulation domain. Near the surface of the device the vapor flow is mostly driven by diffusion, however convection by the air flow starts to dominate at a distance of  $> 11$  cm from the surface, as shown in Supplementary Fig. S4.

### 2.3. Electrical model

Since the most common experimentally measured quantity of a porous nanogenerator is the produced voltage, the solved water flow must be connected to electricity generation. The electrical model used for calculating the electric output from the simulation is an equivalent circuit shown in Fig. 1 (b), where the FEM solution of the water dynamics model is used to calculate the values of the components in the equivalent circuit. The current sources are calculated based on the definition of the streaming current [43]

$$I_s = \int_A u_y \rho_{charge} dA, \quad (14)$$

where  $I_s$  is the streaming current,  $u_y$  is the vertical component of the liquid velocity,  $\rho_{charge}$  the effective charge density and  $A$  the cross sectional area. Instead of solving the integral explicitly, the streaming current is calculated from the volumetric water flux

$$Q = \int_A u_y dA, \quad (15)$$

which is directly obtained from the FEM solution. The water flux is related to the streaming current by a constant factor, which captures the effects of the charge density and pore geometry [44]. The current source values for each of the 1000 source-resistor pairs in the equivalent circuit model are calculated by

$$j_i = Q_i C_j, \quad (16)$$

where  $j_i$  is the  $i$ th current source element,  $Q_i$  the mean volumetric liquid water flux at the corresponding height and  $C_j$  the streaming current coefficient. The streaming current coefficient  $C_j$  is the only free parameter fitted to experimental voltage measurements with a value of  $4.5 \times 10^4 \text{ A s/m}^3$ . Since the equivalent circuit is linear, the impact of the streaming current coefficient on the simulation results is also linear, acting as a constant multiplier on the simulated voltage.

The resistivity of the porous material depends on both the liquid water saturation and the water vapor saturation in the material. Higher water vapor content i.e. higher humidity is known to increase the resistivity [45], while adding liquid water will reduce the resistivity. In order to calculate the produced voltage an empirical model for the resistance of the material was used: the resistance was measured from samples in a humidity controlled chamber, and from samples saturated with liquid water. The measured values are listed in Table 1. The resistance at different positions of the device was then calculated by bilinear interpolation of the measurement data with simulated liquid saturation and relative humidity. When both the current sources and the resistances in the equivalent circuit are known, the electric potential is solved using the matrix form of the node-voltage equation

$$\mathbf{I} = \mathbf{G}\mathbf{V}, \quad (17)$$

where  $\mathbf{I}$  is a vector of the node currents,  $\mathbf{G}$  the conductance matrix and  $\mathbf{V}$  the unknown electric potential vector. The voltage as measured in the experimental device is then given by the difference between the potential of the nodes corresponding to the positions of the contact electrodes. This enables an efficient computation of the voltage measured between arbitrarily positioned electrodes.

## 3. Results and discussion

### 3.1. Electrical response: transient near the water surface

In the initial state for both the simulation and the experiments the device contains no liquid water, and is in equilibrium with the ambient humidity. After the device is placed in water, the capillary pressure forces liquid water into the porous material, leading to evaporation and

increased water vapor concentration. While in a typical application these devices operate in the steady state, in order to verify the accuracy of the simulation the initial transient response to placing a dry device into water was additionally investigated. For that purpose, samples with electrodes placed densely near the water surface were fabricated. As illustrated in Fig. 3 (a), three electrodes, numbered 0–2, are located close to the water surface to investigate the initial transient, and electrode 3 is placed near the top end of the device, in order to measure the voltage generated over the full length of the nanoporous carbon sample. Electrodes 0–2 were measured to be 2 mm apart from each other using an optical microscope, as shown in Supplementary Fig. S2, and the samples were carefully placed in the water so that the water level was halfway between electrodes 0 and 1. The voltage measured between electrodes 1 and 2 in Fig. 3 (b) shows that a strong voltage peak is initially created in this small part of the device, as the water rushes to fill the porous material. The voltage then slowly settles to a lower value as the system approaches steady-state operation. This behaviour is reproduced by the simulation: the sharp voltage peak is generated as the initial water flow rate into the dry device is extremely high compared to the steady state. As the liquid front rises higher and eventually reaches equilibrium, the water flow rate is ultimately limited by the evaporation rate. When the liquid flow rate equalizes over the device, the voltage

distribution also evens out: instead of a high potential gradient over the first few millimeters, in the steady state the voltage is generated over a longer distance with a more shallow gradient as shown in Fig. 4 (h).

### 3.2. Time evolution of the water flow

Figs. 4 (a–e) show the state of the device 34s after being placed into water, which is the time of the peak voltage measured between electrodes 1 and 2 in Fig. 3 b. At this point, the liquid water front has reached 5 mm above the water surface level and covers electrode 2. As the water front climbs higher, the flowrate reduces until the steady state is reached, as the liquid inflow at the bottom of the device is in equilibrium with the evaporation rate.

The capillary pressure, which is responsible for lifting the water into the material according to Eq. 2, presents a constant gradient from the bottom up to the height where most of the water has evaporated. Even though most of the pressure drop and therefore the largest flow velocity are found just above the wetting front, this region has negligible impact on the final power output due to the low volume of liquid water left in the device. In the electrical model the current generation is connected to the volumetric flux, which monotonically reduces as more water is evaporated away. Therefore, majority of the current is produced in the

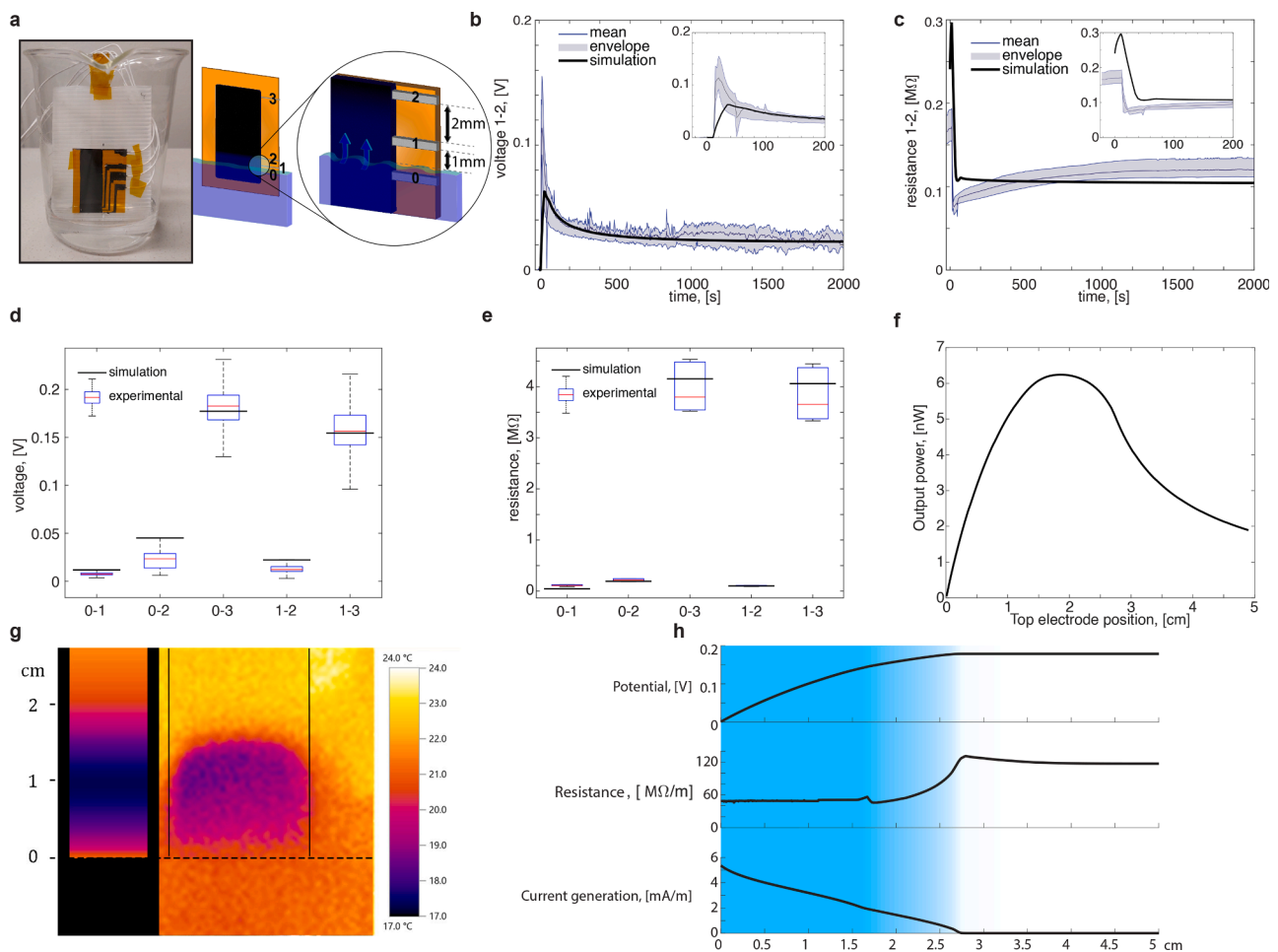


**Fig. 3.** a) Photograph of the experimental setup and a schematic of the electrodes on the samples used for the transient measurements. The samples were measured with the water level between the two bottom electrodes, so that the middle electrode was 1 mm above the surface. b) The transient voltage measured between electrodes 1 and 2. The shaded area shows the mean value and the envelope of extreme values of the experimental data, and the thick line is the simulated result. The inset shows the same data zoomed in on the first 200 s. c) Same as b), for resistance d) The steady state voltages measured between different electrodes. The box plots represent the experimental results and the horizontal black lines the simulated voltages. e) Right: the power supplied by the generator to a matched load as function of the top electrode distance from water surface. f) The simulated power output as function of the top electrode distance from water surface. g) The temperature of the surface of the device at steady state operation. Left: simulation, right: thermal camera image of the device overlaid on a photograph. The dashed line indicates the water surface. h) electrical output of the device at steady state. The blue gradient indicates liquid phase saturation.

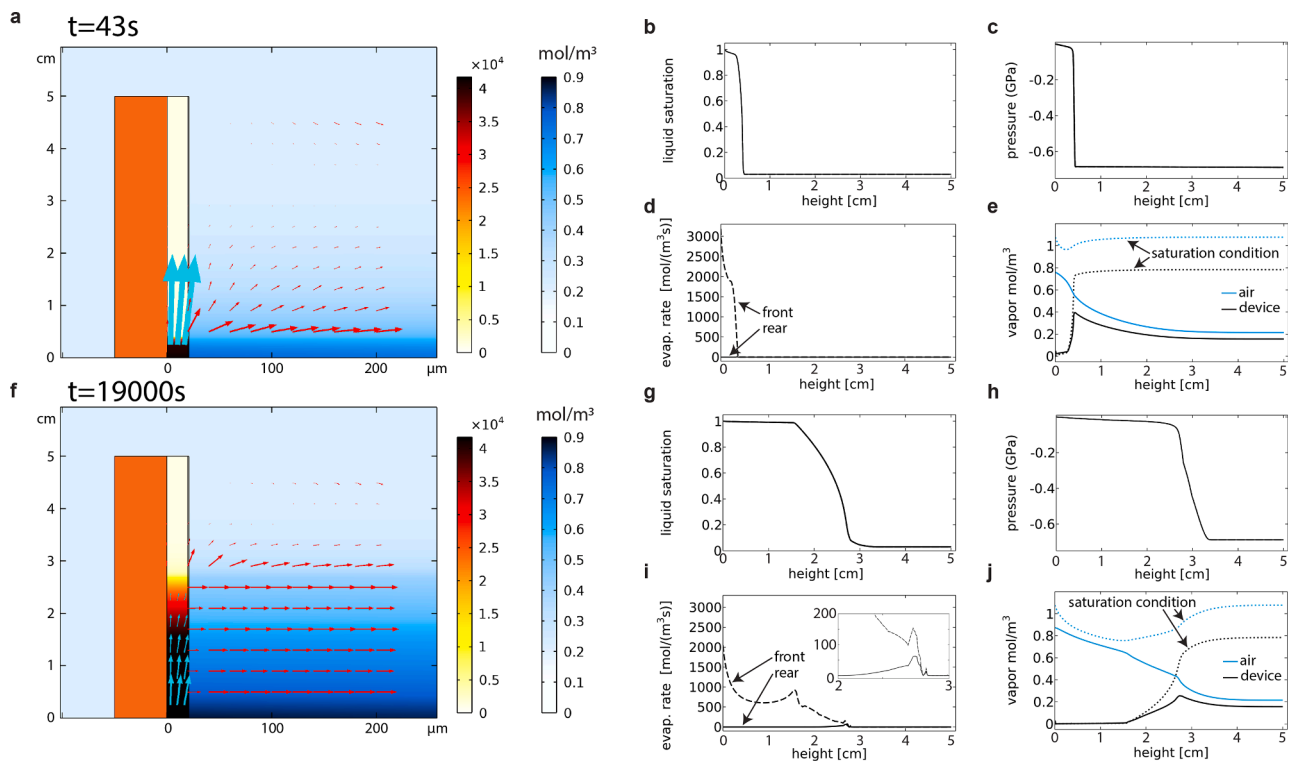


**Fig. 4.** FEM results at the time of peak voltage between electrodes 1 and 2 as seen in Fig. 3 (c) at  $t = 43\text{ s}$  (a–e), and at steady state (g–k). Left: surface colors mark the concentrations, and arrow plots volumetric fluxes. Red surface and blue arrows: liquid water concentration and flux, blue surface and red arrows: water vapor in air. Animation of the time evolution in a) and g) is available in the [Supplementary video 1](#). b) liquid phase saturation, c) pressure from Eq. 2, d) water evaporation rate, e) water vapor concentration and saturation concentration inside the device (black) and in the air immediately outside the device (blue). g–j like b–e, but at  $t = 19000\text{ s}$ . (steady state).

fully saturated section at the bottom of the device as seen in Fig. 3 (h). The wetting front height is clearly defined with no variation between the open front surface and the back surface against the substrate. The water evaporation rate, however, is significantly higher on the front surface, where the liquid is directly exposed to the ambient air than on the rear surface against the Kapton film. While this results in a net liquid flow from the back towards the open surface, the lateral flow does not contribute to the generated electrical power, as the electrodes are separated on the  $y$ -axis only. As the time advances the water rises higher, and the bulk of the porous media that is not exposed to free air becomes fully saturated with the liquid phase. Therefore, inside the material evaporation can only happen close to the wetting front where there is not enough water remaining to keep the pores saturated. In the steady state, this happens at a 2.5 cm height, as seen in the inset in Fig. 4 (j), although the evaporation rate is still minimal compared to the rate on the open surface. In the region that is not saturated by the liquid, the gas phase takes up more volume and can contain more moisture. Fig. 4 (e and j) show how both the saturated vapor concentration and the actual vapor concentration inside the porous material increase above the wetting front. Similarly to the liquid water saturation, the gas phase water vapour concentration is also constant along the depth into the porous material throughout the time evolution. While the evaporation of water is significantly faster on the front surface of the device, the diffusion of the vapor inside the porous material is fast enough to equalize the concentration across the  $20\mu\text{m}$  thickness.

After reaching the steady state shown in Fig. 4 (f–j), the device can be divided into three regions of operation. The bottom 1.5 cm is fully saturated with the liquid phase, and the vapor concentration inside the device is zero due to the lack of air phase volume. The evaporation rate on the front surface is high, limited by the vapor concentration in the air outside the device approaching saturation. It is also notable that the high evaporation rate in this region acts as a negative feedback for the

produced power as the evaporation cools the surrounding air and therefore lowers the saturation vapor concentration according to Eq. 10. While directly measuring the water evaporation rate from the surface of the device is not feasible, an indirect estimate can be made by measuring the effect of evaporative cooling: the temperature of the surface presented in Fig. 3 (g) clearly shows the impact of the cooling effect both in the simulation and the thermal camera image, with the coldest point of the surface at  $5^\circ\text{C}$  below the ambient temperature. Most of the water evaporates at or below 2 cm above the waterline. While the cooling effect is present on the surface immediately above the waterline, the liquid water enters the device at ambient temperature keeping the bottom of the device warm. Comparing the simulated temperature to the thermal camera image shows that the simulation captures both the height and the magnitude of the evaporative cooling in the device accurately. The good match of the simulated cooling effect further shows that the total water evaporation rate and therefore the flow rate through the device in the simulation matches with the experimental case.

In the middle region between 1.5 and 3 cm the water saturation starts to drop and simultaneously the vapor saturation inside the porous material increases. Here, the vapor concentration starts to fall further from the saturation condition, and the evaporation rate is limited by the water activity instead. The activity eventually falls to zero as the liquid saturation reduces, completely stopping the evaporation from taking place. In the top part above 3 cm all of the water has evaporated, and the vapor concentration approaches equilibrium with the ambient humidity of 20%. In the equilibrium, the vapor concentration inside the device is lower than in the air by the factor of the material porosity,  $\varphi = 0.75$ .

### 3.3. Electrical response: steady state

In the steady state, the liquid water inflow rate from the water reservoir is equal to the water vapor outflow rate from the device and

the water saturation inside the device is constant. The measured saturated voltages between different electrode pairs are shown in Fig. 3 (d), alongside the simulated results. The experimental data for the steady state was collected by measuring the voltage and resistance from three different samples over one hour for each pair of electrodes. In steady state operation, most of the voltage is generated in the long section between electrodes 2 and 3, but the voltage over the first two millimeters of the carbon film is still significant. The simulation agrees well with the experimental data over all electrode pairs, however an exact comparison is made difficult by the high variance in the measurements. Although the measurement variance over the short sections at the bottom of the device is relatively low, the measurement accuracy is limited by the uncertainty of the exact position of the water surface relative to the electrodes. Nevertheless, the simulated voltage distribution where the voltage increase is close to linear as function of height is well in line with what has been reported previously [6,19,46].

Fig. 3 (h-j) presents the voltage, resistivity and current generation distributions in a typical 5 cm long device during steady state operation. However, the results in Fig. 3 (f) show that the optimal length for the device is only 2 cm. As seen in Fig. 3 (h) most of the power is produced in the lower part of the device close to the water surface, and the dry top section is only adding extra resistive load. For maximum power output the top electrode should be placed 1.5-2.5 cm above the water surface slightly below the wetting front. Merely a 1 cm deviation of the optimal electrode position can drop the output power by more than 20%. This has significant implications for the optimal design of the device as the wetting front and consequently the optimal electrode position can vary based not only on the porous material, but also on environmental conditions that may change during operation.

A sensitivity analysis comparing the effects of various parameters on the steady state voltage and water front height is shown in Fig. 5: namely, the ambient air flow velocity, the pore size distribution index, the thickness of the carbon film, the evaporation rate constant, the porosity of the carbon material, and the critical pore size. Reducing the external air flow velocity  $u_0$  has a minimal impact on the simulation results until the velocity is close to zero. The assumptions of the laminar flow and no-slip wall condition cause the air flow velocity near the surface of the device to always be extremely low regardless of the average ambient flow velocity, as seen in Fig. 2. This results in diffusion being dominant, and therefore limiting the transport mechanism of water vapor in the air close to the device, even at high flow rates. At lower flow rates, the region dominated by diffusion increases, and at zero velocity the vapor is transported solely by diffusion. This limits the evaporation rate, enabling the water front to reach the top of the device at 5 cm. However, even at 0 m/s velocity the evaporation is not completely stopped, and there is still enough liquid flow to generate only

a slightly reduced voltage. The wetting front position however changes drastically, reaching all the way to the top of the device at 5 cm. This indicates that while the simulation is not sensitive to the exact magnitude of the air flow velocity, some kind of convective transport for the water vapor must be included in the model for accurate results.

Increasing the ambient humidity  $\phi$  has the intuitive effect of reducing the evaporation rate and therefore causing the steady state wetting front to climb higher, eventually reaching the top edge of the device at 60% relative humidity. However, the produced voltage remains constant as long as the device is long enough to allow all of the water to evaporate. Only if the relative humidity is increased all the way to 100%, the evaporation stops completely and no voltage is produced.

Similarly to the air flow velocity, low values of the evaporation rate constant  $K$  in Eq. 9 cause the wetting front to reach the top of the device. However, since unlike for the vapor transport, there is no alternative mechanism for the evaporation, evaporation rates approaching zero drastically limit the total water flow and therefore the produced voltage. Increasing the evaporation rate constant above  $K = 10^4 \text{ s}^{-1}$  has negligible effect as the evaporation rate is constrained by the vapor concentration at the surface becoming saturated according to Eq. 9, and the reaction becomes mass transport limited.

Overall, as long as the total evaporation rate is fast enough that the water does not reach the top of the device, the impact on the produced voltage is small. However, as the water reaches the top, the produced voltage starts to drop rapidly. This could be mitigated by making the device longer, however increasing the length comes with the cost of additional resistive losses. Therefore a design compromise must be made between a short device for maximum power in optimal conditions, and a longer device with lower peak power but less sensitivity to ambient humidity and airflow.

While increasing the porous layer thickness has a linear effect on the total water flux, this increase is not apparent from the produced voltage since it is cancelled out by the assumption that the total resistance follows the equation for a three dimensional uniform conductor

$$R = \rho \frac{L}{A}, \quad (18)$$

where  $R$  is the resistance measured between the electrodes, i.e. the internal resistance of the generator,  $\rho$  the bulk resistivity,  $L$  the distance between the electrodes and  $A$  the cross sectional area of the porous film. The larger cross sectional area allows higher total water flow and therefore higher current, but this is balanced by the reduced resistance resulting in a constant voltage when the thickness is varied. However, since the voltage stays constant, but the generated current increases, thicker devices do generate more power. Therefore, optimizing the layer thickness could offer an easy way to increase the power output of the

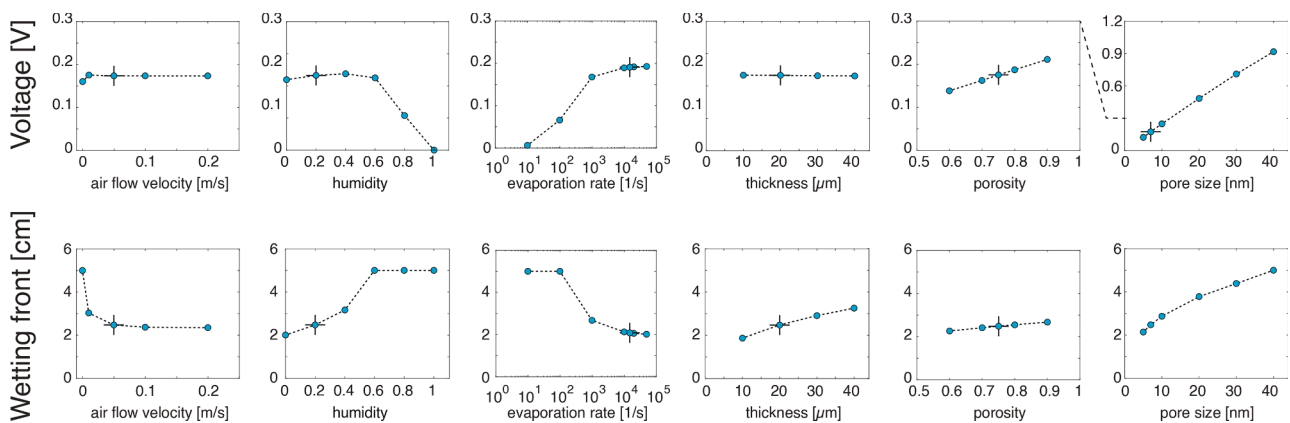


Fig. 5. Sensitivity of the steady state simulation results to variations in input parameters. Top row: impact on voltage between electrodes 0–3. Bottom row: impact on the wetting front position defined as  $S_l < 0.5$ . The crosses mark the default values used for the simulation. Dashed lines are a piecewise linear interpolation for visual clarity.

generator.

The structure of the porous material is described by three parameters: the porosity, the critical pore size, and the pore size distribution index. The pore size distribution index is an effective parameter describing the uniformity of the pore sizes, and the exact value is found to have negligible effect on the simulation result.

The effect of the porosity  $\varphi$  is linear on both the wetting front position and the produced voltage, with higher porosity material creating higher water flow, higher wetting front and more voltage. While the porosity of the material can be measured using pycnometry, this is generally not done in published literature, while simultaneously the reported voltages vary from tens of millivolts [9] to few volts [8]: differences in porosity or pore size could explain some of the variance between published experiments.

Out of all the parameters studied, changing the critical pore radius  $r_c$  has the highest impact on the produced voltage. Compared to the porosity, the critical pore size is exceedingly difficult to estimate experimentally, although microscopy techniques such as SEM can be used to obtain an upper limit on the pore size.

However, the results of the sensitivity analysis are produced under the assumption that all other parameters stay constant when the pore size is changed, while the pore size and porosity are generally not independent of each other. Additionally, since the average distance of the liquid flow from the capillary wall increases, a larger pore size should also result in a lower streaming current coefficient, which would mitigate the predicted voltage increase. Formulae for the streaming current or streaming potential commonly include a geometry factor to account for the pore size and shape [44,47]; however, this factor is generally unknown, and the coefficient is found by fitting a model to experimental results as done in this work. Regardless, our results indicate that a larger pore size would be beneficial and highlight the significant influence of the pore geometry on the voltage compared to the other studied parameters.

#### 4. Conclusions

A multiphysics model combining the capillary action of water in a porous media, evaporation and multiphase mass transport was developed to solve the water dynamics in a porous carbon generator. The solutions were further applied to an electrical equivalent circuit to simulate the streaming current and voltage generation in the porous material. We show that the electricity generation characteristics of a nanoporous carbon film can be simulated to excellent accuracy, most results being within experimental error. Furthermore, the simulation results highlight the importance of accurate characterization when comparing different experimental works, as small variations of material properties such as the pore size can explain observed differences in produced current and voltage. Advanced characterization methods such as ellipsometric porosimetry [48] could be useful in experimentally revealing the exact effect of the porosity and pore geometry on the electrical power output. Finally, our results offer a way to reliably simulate the power output of an evaporation powered nanoporous generator under different configurations and ambient conditions, and show that even small design choices such as electrode positions can have a major impact on the output of the generator.

#### CRediT authorship contribution statement

**L. Hällström:** Conceptualization, Methodology, Software, Validation, Formal analysis, Data curation, Writing - original draft, Writing - review & editing, Visualization. **T. Koskinen:** Methodology, Validation, Investigation, Resources, Data curation, Writing - review & editing, Visualization. **C. Tossi:** Investigation, Writing - review & editing. **T. Juntunen:** Conceptualization, Writing - review & editing, Funding acquisition. **I. Tittonen:** Supervision, Funding acquisition, Writing - review & editing.

#### Declaration of Competing Interest

The authors declare that they have no known competing financial interests or personal relationships that could have appeared to influence the work reported in this paper.

#### Acknowledgements

The authors acknowledge the financial support from the Academy of Finland project 319018. L.H. and T.K. acknowledge funding from the Aalto ELEC doctoral school, and C.T. from the Vilho, Yrjö ja Kalle Väisälä Fund grant issued by the Finnish Academy of Arts and Sciences. T.K. acknowledges the support from the Walter Ahlström foundation. Further thanks go to Dr. Benjamin Wilson for the pycnometry measurements. The pycnometry was done using the Raw Materials research infrastructure by Aalto University School of Chemical Engineering, and other experimental work using the facilities and equipment of Micro-nova Nanofabrication Center. Finally, we acknowledge the computational resources provided by the Aalto Science-IT project.

#### Appendix A. Supplementary data

Supplementary data associated with this article can be found, in the online version, at <https://doi.org/10.1016/j.enconman.2022.115382>.

#### References

- [1] Dao V-D, Vu NH, Yun S. Recent advances and challenges for solar-driven water evaporation system toward applications. *Nano Energy* 2020;68:104324.
- [2] Dao V-D, Vu NH, Dang H-LT, Yun S. Recent advances and challenges for water evaporation-induced electricity toward applications. *Nano Energy* 2021;105979.
- [3] Chen Z, Shi J, Li Y, Ma B, Yan X, Liu M, Jin H, Li D, Jing D, Guo L. Recent progress of energy harvesting and conversion coupled with atmospheric water gathering. *Energy Convers Manage* 2021;246:114668.
- [4] Van der Heyden FH, Bonthuis DJ, Stein D, Meyer C, Dekker C. Electrokinetic energy conversion efficiency in nanofluidic channels. *Nano Lett* 2006;6:2232–7.
- [5] van der Heyden FH, Bonthuis DJ, Stein D, Meyer C, Dekker C. Power generation by pressure-driven transport of ions in nanofluidic channels. *Nano Lett* 2007;7:1022–5.
- [6] Xue G, Xu Y, Ding T, Li J, Yin J, Fei W, Cao Y, Yu J, Yuan L, Gong L, et al. Water-evaporation-induced electricity with nanostructured carbon materials. *Nat Nanotechnol* 2017;12:317–21.
- [7] Quincke G. Ueber die fortführung materieller theilchen durch strömende elektricität. *Ann Phys* 1861;189:513–98.
- [8] Li J, Liu K, Ding T, Yang P, Duan J, Zhou J. Surface functional modification boosts the output of an evaporation-driven water flow nanogenerator. *Nano Energy* 2019;58:797–802.
- [9] Li M, Zong L, Yang W, Li X, You J, Wu X, Li Z, Li C. Biological nanofibrous generator for electricity harvest from moist air flow. *Adv Funct Mater* 2019;29:1901798.
- [10] Qin Y, Wang Y, Sun X, Li Y, Xu H, Tan Y, Li Y, Song T, Sun B. Constant electricity generation in nanostructured silicon by evaporation-driven water flow. *Angew Chem* 2020;132:10706–12.
- [11] Zhou X, Zhang W, Zhang C, Tan Y, Guo J, Sun Z, Deng X. Harvesting electricity from water evaporation through microchannels of natural wood. *ACS Appl Mater Interfaces* 2020;12:11232–9.
- [12] Ding Y, Li S, Tian J, Wang F, Shi Y, Tao X, Wang X, Lei R, Chen X. Cnts/wood composite nanogenerator for producing both steam and electricity. *ACS Appl Electron Mater* 2021.
- [13] Dao V-D, Vu NH, Choi H-S. All day limonium laevigatum inspired nanogenerator self-driven via water evaporation. *J Power Sources* 2020;448:227388.
- [14] Zhang S, Fang S, Li L, Guo W. Geometry effect on water-evaporation-induced voltage in porous carbon black film. *Sci China Technol Sci* 2021;64:629–34.
- [15] Ding T, Liu K, Li J, Xue G, Chen Q, Huang L, Hu B, Zhou J. All-printed porous carbon film for electricity generation from evaporation-driven water flow. *Adv Funct Mater* 2017;27:1700551.
- [16] Liu K, Ding T, Li J, Chen Q, Xue G, Yang P, Xu M, Wang ZL, Zhou J. Thermal-electric nanogenerator based on the electrokinetic effect in porous carbon film. *Adv Energy Mater* 2018;8:1702481.
- [17] Guan H, Zhong T, He H, Zhao T, Xing L, Zhang Y, Xue X. A self-powered wearable sweat-evaporation-biosensing analyzer for building sports big data. *Nano Energy* 2019;59:754–61.
- [18] He H, Zhao T, Guan H, Zhong T, Zeng H, Xing L, Zhang Y, Xue X. A water-evaporation-induced self-charging hybrid power unit for application in the internet of things. *Sci Bull* 2019;64:1409–17.
- [19] Li L, Hao M, Yang X, Sun F, Bai Y, Ding H, Wang S, Zhang T. Sustainable and flexible hydrovoltaic power generator for wearable sensing electronics. *Nano Energy* 2020;104663.

- [20] Zhao F, Guo Y, Zhou X, Shi W, Yu G. Materials for solar-powered water evaporation. *Nat Rev Mater* 2020;1–14.
- [21] Shin S-H, Cheong JY, Lim H, Padil VV, Venkateshaiah A, Kim I-D. Carbon anchored conducting polymer composite linkage for high performance water energy harvesters. *Nano Energy* 2020;104827.
- [22] Xin C, Rao Z, You X, Song Z, Han D. Numerical investigation of vapor-liquid heat and mass transfer in porous media. *Energy Convers Manage* 2014;78:1–7.
- [23] Terzi A, Foudhil W, Harmand S, Jabrallah SB. Experimental investigation on the evaporation of a wet porous layer inside a vertical channel with resolution of the heat equation by inverse method. *Energy Convers Manage* 2016;126:158–67.
- [24] Alomar OR, Mendes MA, Ray S, Trimis D. Numerical investigation of complete evaporation process inside porous evaporator using staggered and non-staggered grid arrangements. *Int J Therm Sci* 2018;129:56–72.
- [25] Alomar OR, Mohammed RR, Mendes MA, Ray S, Trimis D. Numerical investigation of two-phase flow in anisotropic porous evaporator. *Int J Therm Sci* 2019;135: 1–16.
- [26] Wang X, Jia P, Sun S, He X, Lu TJ, Xu F, Feng S. Evaporation-induced diffusion acceleration in liquid-filled porous materials. *ACS Omega* 2021;6:21646–54.
- [27] Li J, Zhang D, Wang N, Chang H. Deep learning of two-phase flow in porous media via theory-guided neural networks. *SPE J* 2021;1–19.
- [28] Chen Y, Choong ET, Wetzel DM. A numerical analysis technique to evaluate the moisture-dependent diffusion coefficient on moisture movement during drying. *Wood Fiber Sci* 1996;28:338–45.
- [29] Halder A, Dhall A, Datta AK. Modeling transport in porous media with phase change: applications to food processing. *J Heat Transfer* 2011;133.
- [30] Datta A. Porous media approaches to studying simultaneous heat and mass transfer in food processes. ii: Property data and representative results. *J Food Eng* 2007;80: 96–110.
- [31] Zhong J, Huang C, Wu D, Lin Z. Influence factors of the evaporation rate of a solar steam generation system: A numerical study. *Int J Heat Mass Transf* 2019;128: 860–4.
- [32] Lynch ME, Ding D, Harris WM, Lombardo JJ, Nelson GJ, Chiu WK, Liu M. Flexible multiphysics simulation of porous electrodes: Conformal to 3d reconstructed microstructures. *Nano Energy* 2013;2:105–15.
- [33] Kong X, Jiang J, Lu D, Liu Z, Wu J. Molecular theory for electrokinetic transport in ph-regulated nanochannels. *J Phys Chem Lett* 2014;5:3015–20.
- [34] Khizhnyak P, Chechetkin A, Glybin A. Thermal conductivity of carbon black. *J Eng Phys* 1979;37:1073–5.
- [35] Rossman R, Smith W. Density of carbon black by helium displacement. *Ind Eng Chem* 1943;35:972–6.
- [36] Martys N, Garboczi EJ. Length scales relating the fluid permeability and electrical conductivity in random two-dimensional model porous media. *Phys Rev B* 1992; 46:6080–90.
- [37] Nishiyama N, Yokoyama T. Permeability of porous media: role of the critical pore size. *J Geophys Res: Solid Earth* 2017;122:6955–71.
- [38] Brennan JK, Bandosz TJ, Thomson KT, Gubbins KE. Water in porous carbons. *Colloids Surf A* 2001;187:539–68.
- [39] A. Webb, *Principles of environmental physics*. by j. l. monteith & m. h. unsworth. edward arnold, sevenoaks. 2nd edition, 1990. pp. xii + 291. price 15.99(32.00 hardback). isbn 0 7131 2931 x, Q J R Meteorol Soc 120 (1994) 1700–1700.
- [40] Millington R. Gas diffusion in porous media. *Science* 1959;130:100–2.
- [41] Millington R, Quirk J. Permeability of porous solids. *Trans Faraday Soc* 1961;57: 1200–7.
- [42] Sallam A, Jury W, Letey J. Measurement of gas diffusion coefficient under relatively low air-filled porosity. *Soil Sci Soc Am J* 1984;48:3–6.
- [43] van der Heyden FH, Stein D, Dekker C. Streaming currents in a single nanofluidic channel. *Phys Rev Lett* 2005;95:116104.
- [44] Kuwano O, Nakatani M, Yoshida S. Effect of the flow state on streaming current. *Geophys Res Lett* 2006;33.
- [45] Tulliani J-M, Inserra B, Ziegler D. Carbon-based materials for humidity sensing: a short review. *Micromachines* 2019;10:232.
- [46] Zhang S, Chu W, Li L, Guo W. Voltage distribution in porous carbon black films induced by water evaporation. *J Phys Chem C* 2021;125:8959–64.
- [47] Luong D, Sprik R. Examination of a theoretical model of streaming potential coupling coefficient. *Int J Geophys* 2014;2014.
- [48] Baklanov BM, Mogilnikov K, Polovinkin V, Dultsev F. Determination of pore size distribution in thin films by ellipsometric porosimetry. *J Vacuum Sci Technol B* 2000;18:1385–91.